Nano Research

Open Access

Research Article

Multi-heterojunction engineering of simple oxide electrolyte for high-performance low-temperature solid oxide fuel cells

Tingdong Gong[1], Zhiwei Wang[1], Wenli Luo[1], Xiaomei Huang[1], Juntao Pan[1], Xiyong Chen[1,2] ✉, Meiran Chen[3], Imran Shakir[4], Xin Tang[2,3], and Xijun Liu[1] ✉

[1] *Guangxi Key Laboratory of Processing for Nonferrous Metals and Featured Materials, MOE Key Laboratory of New Processing Technology for Nonferrous Metals and Materials, School of Resources, Environment and Materials, Guangxi University, Nanning 530004, China*
[2] *Guangxi Key Laboratory of New Rare-earth Materials, Nanning 530000, China*
[3] *College of Material Science and Engineering, Guilin University of Technology, Guilin 541004, China*
[4] *Department of Physics, Faculty of Science, Islamic University of Madinah, Madinah 42351, Saudi Arabia*

Cite this article: *Nano Research*, **2026**, *19*, 94908331. https://doi.org/10.26599/NR.2026.94908331

ABSTRACT: Achieving high performance in solid oxide fuel cells (SOFCs) under low-temperature operation remains hindered by the lack of efficient electrolytes that can simultaneously ensure fast ion transport and negligible electron leakage. Here, we introduce a ternary multi-heterojunction composite electrolyte based on p-type NiO, n-type $Li_{0.25}Sn_{0.75}O_{2-\delta}$ (LS), and $Sm_{0.2}Ce_{0.8}O_{2-\delta}$ (SDC) to testify its high-performance capability in low-temperature SOFCs. The unique configuration integrates two p–n and one n–n junctions, which can promote the oxygen ion transport while eliminating electronic short-circuiting. The optimized NLS–SDC 6:4 heterostructure (in mass ratio, and NLS stands for the NiO–LS composite precusor prepared in molar ratio of 8:9) achieves a record of an ionic conductivity around 0.348 $S \cdot cm^{-1}$ and a peak power density (PPD) of 916 $mW \cdot cm^{-2}$ at 550 °C, and a long-term stability of over 280 h operation at 150 $mA \cdot cm^{-2}$. Multi-scale characterizations coupled with the density functional theory analyses confirm that the interfacial band alignment and oxygen vacancy enrichment synergistically drive the exceptional ion transport properties. This study highlights multi - heterojunction engineering of simple oxides as a versatile and scalable strategy for next-generation SOFC electrolytes, with broad implications for solid oxide electrolysis, solar energy conversion, and selective ion-conducting membranes.

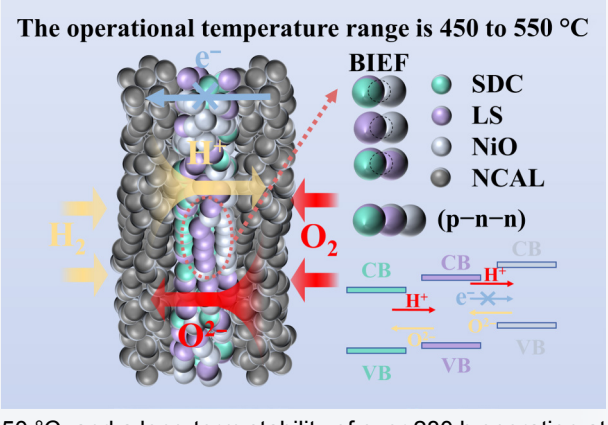

KEYWORDS: low-temperature ceramic fuel cells, simple oxides, multi-heterojunction composite electrolyte, long-term stability

1 Introduction

The rapid growth of global energy demand calls for sustainable and efficient energy conversion technologies. Among various candidates, proton exchange membrane fuel cells (PEMFCs) and solid oxide fuel cells (SOFCs) have attracted wide attention due to their high efficiency and environmental compatibility [1–3]. Conventional SOFCs, however, typically operate at 800–1000 °C, imposing stringent requirements on material stability, sealing, and system safety. Reducing the operating temperature to the intermediate or low-temperature regime (< 600 °C) is therefore a key challenge for achieving practical deployment of SOFCs [4, 5]. A major bottleneck lies in developing electrolytes that simultaneously offer high ionic conductivity, low electronic leakage, and long-term stability under these conditions.

The concept of semiconductor heterojunction electrolytes offers a promising route to address this challenge [6, 7]. Unlike conventional electronically insulating electrolytes, these systems exploit built-in electric fields (BIEFs) at semiconductor heterointerfaces to suppress electron transport while promoting ion mobility [6–11]. Several binary p–n heterojunction

Received: September 15, 2025; **Revised:** November 30, 2025
Accepted: December 10, 2025

✉Address correspondence to Xiyong Chen, xiyongchen@gxu.edu.cn; Xijun Liu, liuxjtjut@163.com

systems, such as $Sm_{0.2}Ce_{0.8}O_{2-\delta}$ (SDC)–$La_{0.6}Sr_{0.4}Co_{0.2}Fe_{0.8}O_{3-\delta}$ (LSCF) and SDC–$SrCo_{0.8}Nb_{0.1}Ta_{0.1}O_{3-\delta}$ (SCNT), have been demonstrated, exhibiting superior ionic conductivity and fuel cell performance compared with traditional yttrium-stabilized zirconia (YSZ) and SDC at reduced temperatures [7, 8]. However, their long-term stability remains insufficient, with most systems showing substantial degradation within ~ 50 h of operation [7, 9–11]. Moreover, the electric field strength of simple binary heterojunctions is often inadequate to fully block electronic leakage, limiting further performance gains.

Multicomponent semiconductor heterostructures, incorporating more than two phases, can generate stronger BIEFs and richer interfacial environments than binary systems [12, 13]. The coexistence of multiple p–n and n–n junctions has the potential to further suppress electronic conduction, reduce the activation energy (E_a) for ion transport, and stabilize oxygen vacancy distributions. The p–n heterointerface induces intense electron scattering, which effectively enhances the selectivity of ions conduction channels [14].

In this study, we report a ternary heterojunction composite electrolyte composed of p-type NiO and n-type $Li_{0.25}Sn_{0.75}O_{2-\delta}$ (LS) and SDC. The choice of materials was guided by the need to integrate a well-known p-type phase (NiO), an n-type phase with a wide bandgap for strong band bending (LS), and an n-type phase known for its excellent ionic conduction (SDC). The multi-heterojunction system integrates two p–n interfaces and one n–n interface, where the n–n junction exerts a significant enhancement effect on the p–n junctions. Specifically, the additional BIEF formed at the n–n interface couples with the electric fields at the p–n interfaces. This coupling not only expands the effective range of the space charge region but also optimizes the charge distribution at the interfaces through synergistic modulation of the band structure [9, 15–17]. On one hand, this coupling mechanism enhances the ion migration capability; on the other hand, the superposition of band bending further suppresses electron transport, thereby strengthening electron blocking. Meanwhile, the multi-interface configuration provides more abundant active sites for the formation and stabilization of oxygen vacancies, effectively regulating their formation energy and distribution stability [18–22]. As a result, more efficient and stable ion transport channels are established (see Scheme 1). Density functional theory (DFT) calculations and spectroscopic characterization further confirm that the increased oxygen vacancies and decreased formation energy of oxygen vacancy enable a rapid ion transport in the ternary system. This work establishes multi-heterojunction engineering as an effective strategy for developing durable electrolytes for low-temperature SOFCs (LT-SOFCs).

2 Results and discussion

2.1 Structure and heterostructure interface

The synthesis methods for NiO–LS–SDC (NLS) and NLS–SDC composites are detailed in the Electronic Supplementary Material (ESM). Figures 1(a)–1(c) showcase the crystal structures of the ternary material system, LS, NiO, and SDC, which form the multi-heterojunction composite. Figure 1(d) reveals the characteristic diffraction peaks of both LS and NiO in the X-ray diffraction (XRD) patterns of NLS and NLS–SDC. Similarly, the diffraction

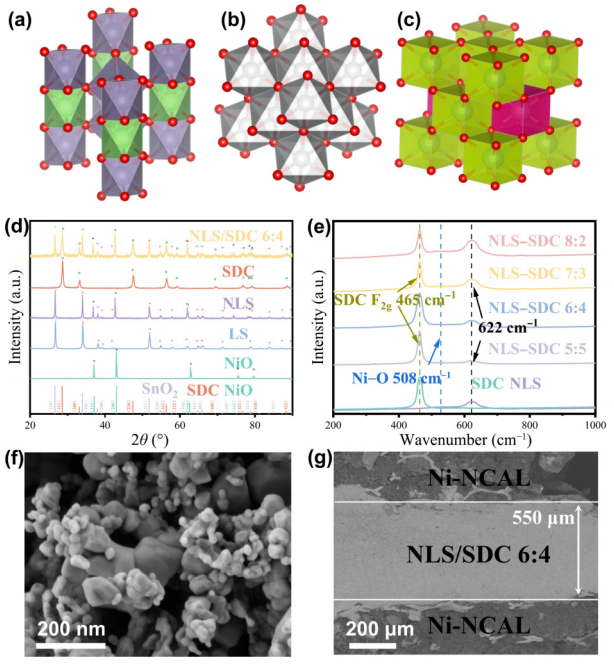

Figure 1 ((a)–(c)) The crystal structures of (a) LS, (b) NiO, and (c) SDC. (d) The XRD patterns of NiO, LS, NLS, SDC, and NLS–SDC 6:4. (e) Raman spectra of NLS–SDC (8:2, 7:3, 6:4, and 5:5). (f) Field emission SEM image of NLS–SDC 6:4 surface and (g) the cross-sectional view of the cell after cell evaluation.

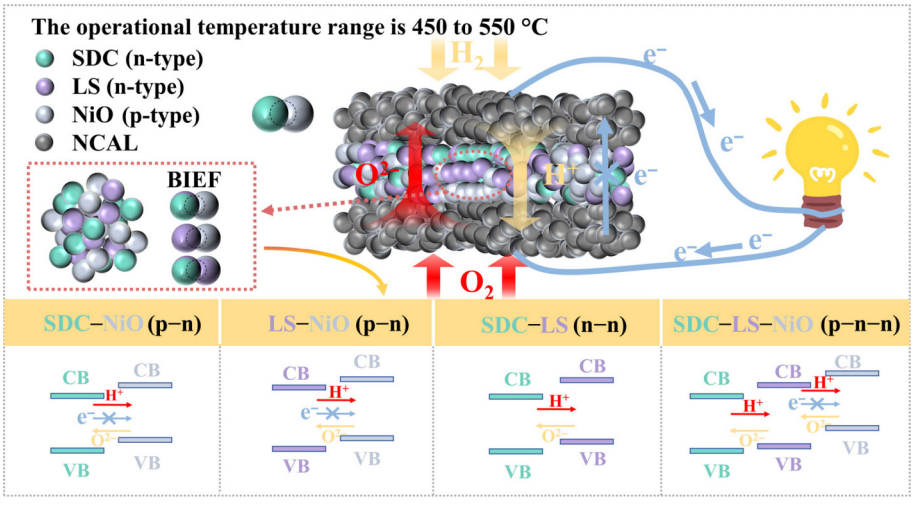

Scheme 1 Fuel cells with an NLS–SDC composite electrolyte and the operating mechanism of the triple heterojunction.

patterns of LS–SDC and NiO–SDC exhibit characteristic peaks of LS and NiO (Fig. S1(a) in the ESM). All reflections are indexed to the tetragonal rutile structure of SnO_2 (PDF#41-1445), the cubic rock-salt structure of NiO (PDF#89-7130), and the cubic fluorite structure of SDC (PDF#97-002-8792). Analyses of Figs. S1(b)–S1(e) in the ESM collectively demonstrate successful Li incorporation into the SnO_2 lattice and formation of a stable NLS–SDC. The material maintains robust structural integrity and thermochemical stability at the operating temperatures (450–550 °C). These results confirm that Li occupies SnO_2 lattice sites, but note unit cells in NLS materials, establishing NLS as a dual-phase composite formed by physical mixing of NiO and LS.

Figure 1(e) shows the Raman spectra of SDC, NLS, and their composites with different ratios excited by a 532 nm laser, presenting multiple significant characteristic peaks. These peaks correspond to the symmetric stretching vibration of Ce–O–Ce (465 cm^{-1}) [23], Ni–O vibration (508 cm^{-1}), and overlapping vibration signals of Li–O and Sn–O (622 cm^{-1}), respectively. No other characteristic peaks appeared in the spectra, indicating that no new chemical bonds were formed in the composites. As the SDC content increased, the peak intensities corresponding to the overlapping vibration of Li–O and Sn–O are gradually weakened, while that corresponding to the Ce–O–Ce vibration gradually strengthens, confirming the coexistence of SDC and NLS in the heterostructure. Figure S2 in the ESM demonstrates that the peaks at 508, 585, and 633 cm^{-1} correspond to Li–O and Sn–O vibrations. The Raman spectra show no formation of new chemical bonds. Combined with XRD results, all data confirm excellent chemical stability in the NLS–SDC heterostructured composite material.

Figure 1(f) shows the scanning electron microscopy (SEM) image of the NLS–SDC 6:4 composite powder material. It can be seen that the powder particles are uniformly distributed, with particle sizes ranging from 20 to 150 nm. Figure 1(g) is the cross-sectional view of the cell after cell performance evaluation. It can be clearly seen that the cross-section of the cell has a sandwich structure of Ni-NCAL (NCAL stands for $Ni_{0.8}Co_{0.15}Al_{0.05}LiO_{2-\delta}$, cathode)–NLS–SDC 6:4 (electrolyte)–Ni-NCAL (anode). The thickness of the electrolyte is approximately 550 μm. Figure S3 in the ESM shows the energy-dispersive X-ray spectroscopy (EDX) of the main elements selected at the cell interface. The main elements Li, Ni, Ce, Sm, Sn, and O of the heterostructure composite electrolyte are uniformly distributed throughout the electrolyte region without obvious agglomeration.

Experimental results indicate that the microstructure of NLS–SDC heterostructure composites plays a crucial role in the efficient electrochemical transport of ions. To determine the detailed morphology and interface distribution of the samples, microstructural analysis of the composites was performed using high-resolution transmission electron microscopy (TEM). Figure 2(a) shows the microstructure of LS materials on the $(1\bar{1}0)$ crystal plane and their corresponding fast Fourier transform (FFT) patterns. The spacings along the [110] and [111] crystal directions are calculated as 3.34 and 2.31 Å, respectively. While for NiO materials on the $(01\bar{1})$ plane, as shown in Fig. 2(b), the lattice spacings along the [111] and [200] crystal directions are identified as 2.42 and 2.11 Å, matching the literature values [24]. Similarly, Fig. 2(c) shows the SDC materials on the $(1\bar{1}0)$ plane, and the lattice spacings along the [220] and [111] crystal directions are estimated as 1.91 and 3.12 Å, in good agreement with the reported data [14]. Figure 2(d) shows the heterojunction interface formed by the (110) crystal plane of LS and the (200) crystal plane of NiO. As for the NLS–SDC composites, particles of LS, NiO, and SDC (three-phase materials) interact with each other, forming well-distributed heterointerfaces between particles, as shown in Fig. 2(e). Figure S4 in the ESM shows the elemental distribution in the triple-phase boundary region, where each element is predominantly located within its respective grain regions. When grains of different materials come into contact to form heterointerfaces, in which lattice mismatch induces localized lattice distortion accompanied by alterations in lattice parameters. Such structural distortion perturbs the occupancy stability and migration behavior of oxygen atoms within the lattice, thereby facilitating the release of originally stable

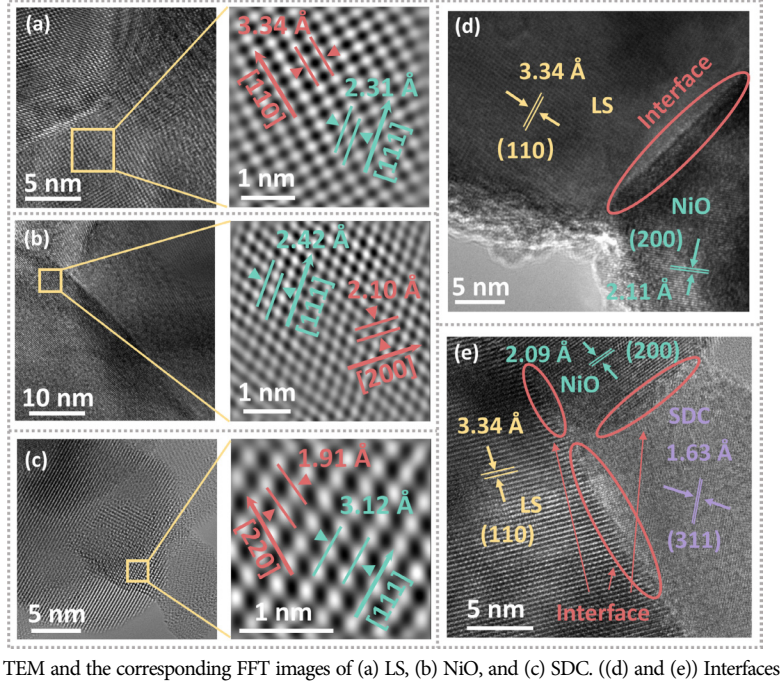

Figure 2 ((a)–(c)) High-resolution TEM and the corresponding FFT images of (a) LS, (b) NiO, and (c) SDC. ((d) and (e)) Interfaces in the (d) NLS and (e) NLS–SDC heterostructure, along with their corresponding lattice spacings.

oxygen atoms from their lattice sites and promoting the formation of oxygen vacancies [25–27]. These heterointerfaces generate multiple different types of heterojunctions, which eventually contribute to the increase in ionic conductivity and the suppression of electronic conductivity of the material, and thereby the performance improvement of fuel cells, as discussed later.

2.2 Fuel cell performance and electrochemical impedance spectroscopy (EIS) evaluation

Different from traditional heterojunction electrolyte fuel cells, this study adopted a three-phase semiconductor composite electrolyte material for LT-SOFC investigation. Current–voltage (*I–V*) and current–power density (*I–P*) tests were conducted to evaluate the electrochemical performance of the fuel cells using various individual prepared components as electrolytes. Figure 3(a) presents the *I–V–P* performance of fuel cells with different electrolyte materials measured in H_2/air atmosphere at temperatures ranging from 450 to 550 °C. The results demonstrate that the NLS–SDC 6:4 composite exhibits superior performance compared to other electrolytes. Corresponding *I–V* and *I–P* characteristics for fuel cells employing NLS–SDC (7:3 and 5:5), NiO–SDC 6:4, and LS–SDC 6:4 as electrolytes under identical conditions can be found in Figs. S5(a)–S5(d) in the ESM.

The peak power densities (PPD) for fuel cells with NiO–SDC and NLS electrolytes were only 282 and 447 mW·cm^{-2} at 550 °C, respectively. For the NiO–SDC composite electrolyte, the relatively

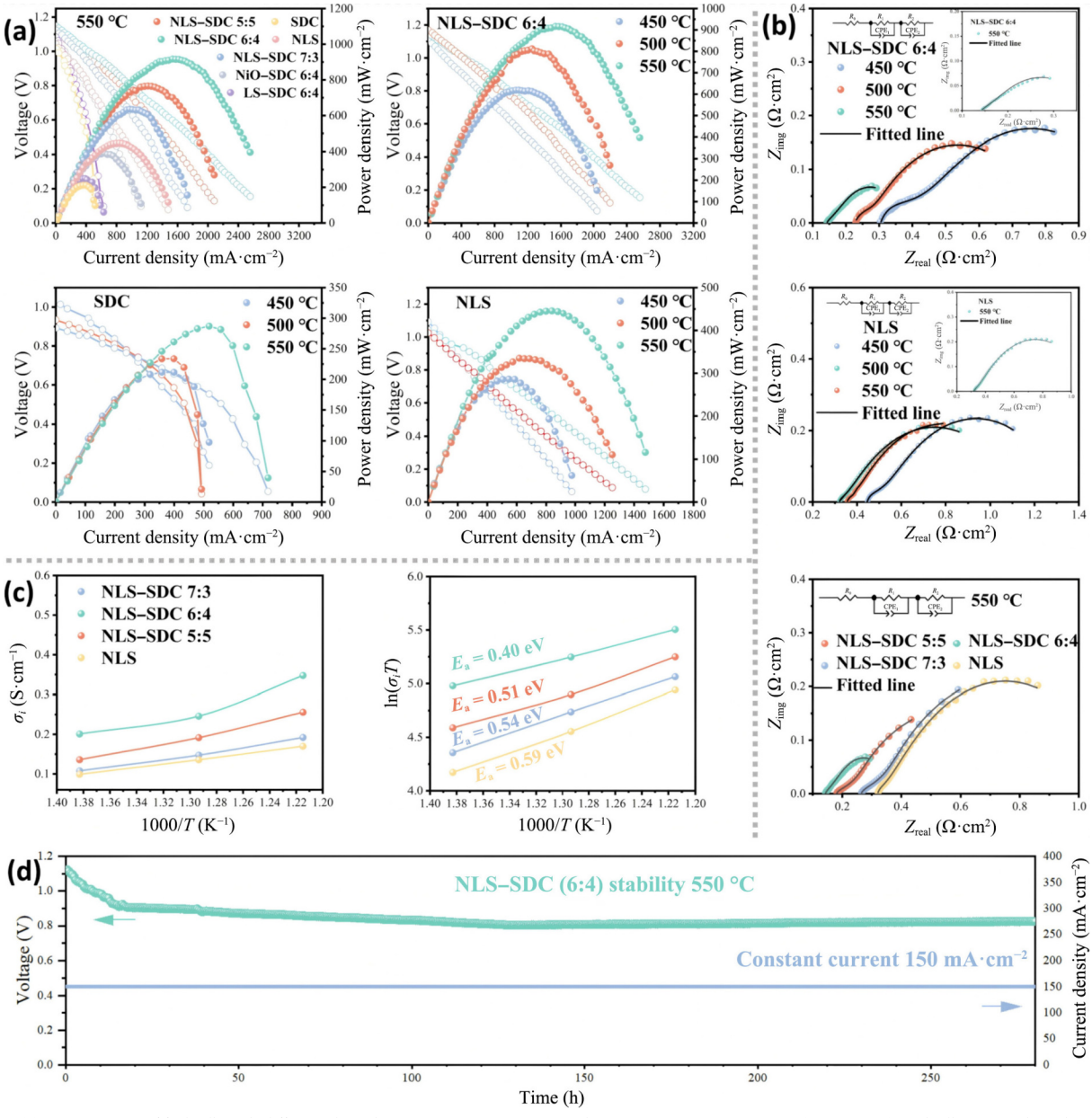

Figure 3 (a) *I–V–P* curves of fuel cells with different electrolytes, NLS–SDC 6:4, SDC, and NLS at varying temperatures (450–550 °C), with all tests conducted in a H_2/air atmosphere. (b) Electrochemical impedance spectra of NLS–SDC 6:4 and NLS within the working temperature range of 450–550 °C, along with those of NLS–SDC (5:5, 6:4, and 7:3) and NLS at 550 °C. (c) Temperature-dependent ionic conductivities and diffusion activation energies of NLS–SDC (5:5, 6:4, and 7:3) and NLS. (d) Long-term operation stability test of the fuel cell with NLS–SDC heterostructure electrolyte at a constant current density of 150 mA·cm^{-2} under the operating temperature of 550 °C in a H_2/air environment.

poor ionic conductivity and high diffusion activation energy at low temperatures (450–550 °C) (Fig. S6(b) in the ESM) are the main drawbacks. Furthermore, the electrolyte material was not well sintered when applied in the semiconductor fuel cell evaluation, and the non-dense construction would increase the resistance to ionic conduction. While for NLS, the relatively low PPD is mainly due to the insufficient ionic conductivity of LS and the stable chemical properties of NiO semiconductor oxides [24, 25]. Additionally, the corresponding conduction and valence band (VB) positions of LS and NiO semiconductors are close (see Section 2.5), leading to poor performance of fuel cells with NLS as the electrolyte. However, by mixing SDC and NLS to form an NLS–SDC ternary composite electrolyte, the fuel cell performance was undoubtedly improved regardless of the ratio of NLS and SDC in the composite electrolytes at all temperatures. Notably, fuel cells with any composite material (except SDC) as the electrolyte exhibit an open circuit voltage (OCV, V_{OC}) higher than 1.0 V at 550 °C. A high OCV indicates effective gas leakage suppression and electronic short-circuiting, which is a prerequisite for efficient fuel cell operation. The combination of high OCV and superior fuel cell performance confirms the feasibility of constructing semiconductor heterojunctions as electrolytes.

By constructing heterojunction interfaces of NiO–LS, NiO–SDC, and LS–SDC, directional optimization of ion transport paths is achieved [25, 26]. The p–n heterojunctions suppress electronic conductivity through the space charge effect, fundamentally solving the electron leakage problem of traditional electrolytes [10, 27]. Meanwhile, it is noteworthy that a Schottky junction (SJ) is successfully constructed between surface metallic Ni and semiconductor NLS–SDC (Fig. S13 in the ESM and its analysis in the ESM). Partial BIEF still exists at the heterointerface, which can still block electron leakage. This is evidenced by the OCV of the LS–SDC material remaining greater than 1 V at 550 °C (Fig. 3(a)) [27, 28]. Experiments show that the PPD of the NLS–SDC 6:4 heterojunction electrolyte reaches 916 mW·cm^{-2} (H_2/air) at 550 °C.

EIS uses the equivalent circuit model $LR_{ohm}(R_{gb}//CPE_{gb})(R_e//CPE_e)$ to quantify the impedance contributions in each frequency domain. Herein, L represents the inductive effect in the high-frequency region (originating from wire or contact impedance); R_{ohm} is the bulk Ohmic resistance (including the electrolyte and electrode contributions); and R_{gb} and R_e correspond to the grain boundary resistance and electrode interface charge transfer resistance, respectively; constant phase element (CPE, $Z_{CPE} = (Q(j\omega)^n)^{-1}$, $0.5 \le n \le 1$) is used to describe the non-ideal capacitive behavior of grain boundaries and electrodes [25, 29], where Z_{CPE} stands for the complex impedance of CPE, Q for the admittance constant, ω for the angular frequency, j for the imaginary unit, and n for the exponent describing the deviation of CPE from an ideal capacitive behavior. Detailed fitting parameters are shown in Table S2 in the ESM.

EIS analysis reveals the charge transport properties and composition dependence of NLS and NLS–SDC heterostructure composites. The EIS of fuel cells with different ratios and NLS as electrolytes at 550 °C is shown in Fig. 3(b). Under the test condition of 550 °C, R_{ohm} of NLS is about 0.318 Ω·cm^2, while NLS–SDC heterostructures with different mass ratios show significant differences, 0.183, 0.140, and 0.267 Ω·cm^2 for NLS–SDC at ratios of 5:5, 6:4, and 7:3, respectively. The overall electrical conductivity (σ) can be derived from Eq. (1) [30]. Notably, R_{ohm} of NLS–SDC 6:4 reaches the minimum value with its conductivity increased to 0.714 S·cm^{-1}, which is 127% higher than that of NLS (approximately 0.314 S·cm^{-1}). This optimization is attributed to the three-dimensional interpenetrating conductive network formed at the heterointerface. The overlapped energy band of NLS–SDC extends the effective conduction length compared to NLS materials. Additionally, as provided by the DFT calculation later, the ternary multi-heterojunction configuration could lower the oxygen vacancy formation energy. Both effects are considered beneficial for increasing the density of electrochemically active sites to promote the oxygen ion transport through the electrolyte

$$\sigma = \frac{l}{R_{ohm}S} \tag{1}$$

where l is the thickness of the electrolyte and S is the effective area of the electrolyte.

Further analysis of the R_{gb} and R_e reveals that both R_{gb} (about 0.131 Ω·cm^2) and R_e (about 0.133 Ω·cm^2) of NLS–SDC 6:4 are lower than those of other NLS–SDC composites and NLS (R_{gb} = 0.289 Ω·cm^2, R_e = 0.702 Ω·cm^2). Based on the above EIS spectrum and resistance parameter analysis, it is known that NLS–SDC heterojunction single cell exhibits optimal ionic conduction characteristics and fuel cell output performance at a 6:4 compositional ratio. Studies show that the composite effect of such semiconductor heterojunctions enhances ionic conductivity through a two-stage mechanism. First, the energy band offset between NLS and SDC induces the recombination of interfacial space charge layers, alleviating the oxygen vacancy depletion effect (such as the suppression of interfacial dopant segregation observed by Xia and co-workers in similar systems) [31]. Second, the LS–NiO–SDC multiphase interface generates structural disorder (the increased disorder of interfacial oxygen distribution reported by Lee et al.) [32], promoting the improvement of oxygen vacancy mobility. Although the interfacial oxygen aggregation model proposed by Zhu et al. can partially explain the conduction enhancement [33, 34], the current study still lacks quantitative characterization of interfacial atomic reconstruction kinetics and lattice strain relaxation in the NLS–SDC system, and DFT calculations are thereby necessary to further reveal the heterointerfacial–conductivity correlation mechanism.

The electrolyte resistance ($R_{electrolyte}$) was approximated from the linear region of the I–V polarization curves, in which the Ohmic polarization in electrolyte dominates in most electrochemical cells [14]. The ionic transport properties of NLS–SDC heterostructures were systematically evaluated by combining the absolute cell resistance (Eq. (2)) and ionic conductivity (σ_{ion}, Eq. (3)) [8, 28]

$$R_{electrolyte} = \frac{V_{ohm}}{I_{ohm}} \tag{2}$$

$$\sigma_{ion} = \frac{l}{R_{electrolyte}S} \tag{3}$$

where V_{ohm} and I_{ohm} are the absolute voltage and current measured during the cell performance evaluation, respectively.

As shown in Fig. 3(c) and Figs. S6(a) and S6(b) in the ESM, experiments indicate that the ionic conductivity of NLS–SDC 6:4 reaches 0.348 S·cm^{-1} at 500 °C, which is significantly higher than that of other composite materials and SDC. A high OCV (V_{OC} > 1.1 V) further verifies the suppression effect of the heterostructure on electron leakage, indicating that ion transport dominates the electrochemical behavior [35, 36]. Lateral comparison shows that

the ionic conductivity of NLS–SDC 6:4 at 550 °C is much higher than that of typical electrolyte materials, gadolinium-doped ceria (GDC, 0.04 S·cm^{-1}@700 °C), YSZ (0.13 S·cm^{-1}@1000 °C), and GDC-YSZ composite films (0.01 S·cm^{-1}@1000 °C), confirming its technical advantages in intermediate and low-temperature fuel cells [37]. The high ionic conductivity enhancement of NLS–SDC heterostructures can be attributed to the dual optimization effect of the interfacial conduction mechanism. On one hand, the three-dimensional percolation network formed at the heterointerface significantly reduces the Ohmic resistance and grain boundary resistance [36]. On the other hand, the oxygen vacancy concentration gradient in the interface region induces a low activation energy ion transport path (E_a = 0.4 eV, see Fig. 3(c)). The diffusion activation energy is evaluated by using Eq. (4) [37]

$$\sigma_{ion} T = A e^{-(E_a/k)} \quad (4)$$

where T is the absolute temperature, A is the pre-exponential component, and k is the Boltzmann constant.

Compared with other compositions, the high ionic conductivity and low diffusion activation energy of the NLS–SDC 6:4 composite jointly indicate that the multi-type heterojunctions (p–n–n) demonstrate enhanced electron blocking and facilitated ion transport. This result confirms that the multicomponent semiconductor heterojunction composites (containing more than two constituents) benefit from their diverse heterojunction interfaces. The remarkable cell performance of NLS–SDC serves as compelling evidence for the validity of the proposed strategy in this work (Table S3 in the ESM).

2.3 Long-term operational stability

Heterostructure electrolytes constructed based on p-type and n-type semiconductor materials provide a new technical path for fuel cell design through the strategy of precise regulation of interfacial energy band alignment. Through energy band gradient regulation and interfacial polarization optimization, this design not only significantly enhances the ionic conduction performance of electrolyte materials but also achieves sustained stability of power output and long-term operational reliability at the device level. Experimental verification shows that the fuel cell device with the Ag/Ni-NCAL/NLS–SDC/NCAL-Ni/Ag composite structure can maintain a stable output voltage after continuous operation for more than 250 h under constant current density in a H_2/air environment at 550 °C (Fig. 3(d)), with a maximum duration of 280 h. The long-term stability test results for the cells constructed with single p–n junction heterostructures based on binary composite materials, such as NiO–SDC 6:4 and NiO–LS (NLS), are presented in Figs. S5(e) and S5(f) in the ESM for comparison. The NLS composite maintained a stable output voltage for approximately 56 h under constant current density operation. This limited stability is primarily attributed to the absence of effective ion transport channels as provided by the SDC phase, resulting in insufficient ion migration pathways. The NiO–SDC 6:4 composite exhibits a moderate ionic conductivity, yet the small band offset between NiO and SDC is insufficient to suppress significant electronic conduction. Consequently, both the peak power output and long-term stability of the full cell are significantly lower than those achieved with the ternary heterojunction composite material. Despite the relatively fast but limited cell performance degradation for the ternary composite-electrolyte cell, its overall operational stability significantly outperforms those of the traditional biphasic composite heterostructure electrolyte systems as reported so far.

The rapid voltage drop during the initial test phase (0–18 h) is supposed to be related to the insufficient thermal equilibration of fuel cell components and incomplete heterostructure formation, leading to elevated overall Ohmic resistance, since the cells were prepared simply from the mechanical pressing of the isolated powders without extremely high temperature sintering. Once the heterostructure reaches macroscopic stability with synchronized polarization stabilization, the voltage degradation decelerates. Concurrently, the operating temperature was significantly lower than the sintering temperature, which allows the gradual release of mechanical stress from cell fabrication, which potentially further lowers the voltage drop rate. The slight voltage recovery after 130 h could be attributed to the increased grain density in the composite electrolyte under the prolonged operation at 550 °C. This, to some extent, improves the internal ionic conductivity and reduces the Ohmic resistance, triggering transient voltage recovery [38]. Experiments show that the NLS–SDC 6:4 composite electrolyte can maintain relatively stable performance after initial adjustment under operating conditions of 550 °C and 150 mA·cm^{-2}, with good long-term operational stability. Although the voltage drops significantly in the initial stage, it can still remain relatively stable afterward, which is favorable for the practical applications of fuel cells. XRD analysis (Fig. S1(c) in the ESM) revealed the formation of impurity phases other than NiO, LS, and SDC in the electrolyte after long-term cycling. This finding provides direct evidence of deterioration at the electrolyte–electrode interface during prolonged operation, accompanied by the precipitation of detrimental phases. Such an interfacial degradation mechanism severely compromises the structure and stability of the heterogeneous interface, which is one of the reasons for the gradual performance decay of the full cell. This observation is in agreement with a mainstream factor widely recognized in Refs. [39, 40]. However, the sophisticated understanding of such performance degradation still requires further investigation.

2.4 Elemental and oxygen vacancy analysis

To verify the high ionic conductivity at the interface in heterostructures, this work performed X-ray photoelectron spectroscopy (XPS) analysis to investigate the chemical states of quantum number distribution in the prepared materials. Figure S7(a) in the ESM shows the complete XPS spectra of NiO, LS, NLS, SDC, and NLS–SDC 6:4. The key contributions and analyses of Ni, Sn, Ce, and O are elaborated and described in detail in Fig. 4 [41]. As shown in Fig. 4(a), the main peak positions of Ni-2p in all Ni-containing samples are concentrated in the range of 855–870 eV, indicating that Ni in the three materials mainly exists in the +2 valence state. More specifically, Ni-2p$_{3/2}$ and Ni-2p$_{1/2}$ are located at 852.7 and 871.5 eV, respectively (the peak spacing between Ni-2p$_{3/2}$ and Ni-2p$_{1/2}$ is about 19.7 eV, consistent with spin-orbit splitting characteristics) and are represented by two partially overlapping peaks. Additionally, Ni-2p generally has two different valence states as Ni^{2+} and Ni^{3+} [42], which are well fitted. It should be noted that NiO presents the strongest satellite peak intensity, demonstrating the typical high-spin state characteristic of Ni^{2+} in NiO (d^8 electron configuration). For NLS and NLS–SDC, it is found that the peak intensities and percentages of Ni^{2+} and Ni^{3+} differ in each sample, and the overall Ni-2p peak shifts slightly towards a higher energy level when compared to NiO. The formation of heterostructures causes changes in the oxidation state of Ni-2p and makes Ni-2p present in mixed oxidation states (Ni^{2+} and Ni^{3+}). Therefore, the oxidation state regulation of Ni-2p (Ni^{2+} oxidized to Ni^{3+}) and the

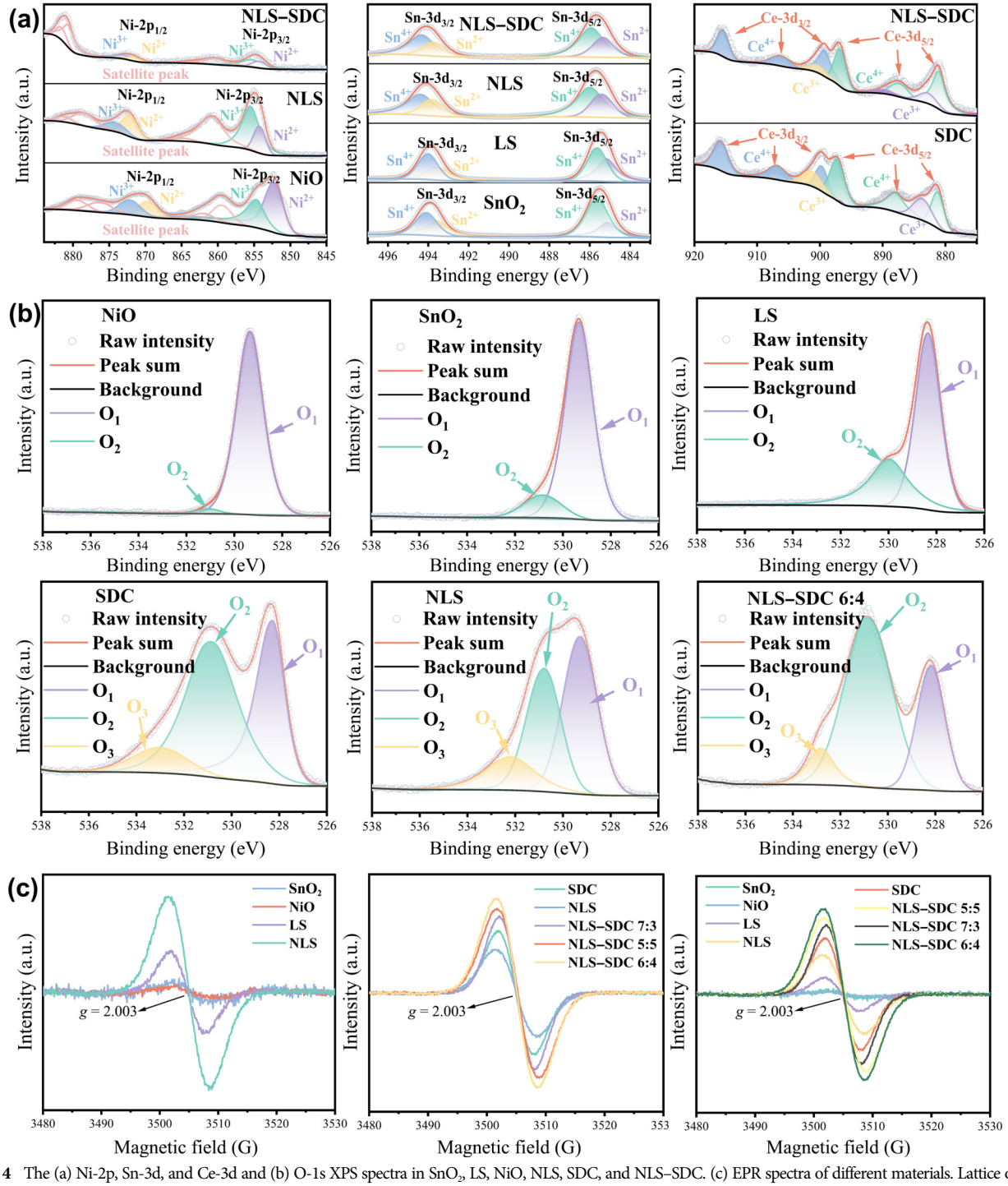

Figure 4 The (a) Ni-2p, Sn-3d, and Ce-3d and (b) O-1s XPS spectra in SnO_2, LS, NiO, NLS, SDC, and NLS–SDC. (c) EPR spectra of different materials. Lattice oxygen, oxygen vacancies, and adsorbed hydroxyl groups are abbreviated as O_1, O_2, and O_3.

construction of heterostructures lead to the alteration of the electronic structure. Similarly, the XPS analysis of Sn, presented in the ESM, also demonstrates the electronic structure modifications induced by the construction of heterostructures (Fig. 4).

The sub-peaks of Ce-$3d_{3/2}$ are assigned to 881.4, 887.7, and 987.1 eV, while Ce-$3d_{5/2}$ are located at 899.8, 906.8, and 915.9 eV, which are characteristic spin-orbit splitting peaks of Ce [43]. Generally, Ce-3d has two different valence states, such as Ce^{3+} and Ce^{4+}, and they are well fitted in the materials under study. It can be clearly seen that the peak intensities and percentages of Ce^{3+} and Ce^{4+} differ among the samples. NLS–SDC materials have a higher proportion of Ce^{3+}, while SDC materials are dominated by Ce^{4+}, with a slight binding energy shift at around 0.24 eV towards a higher energy level. This indicates that heterostructure formation causes changes in the oxidation state of Ce-3d and makes Ce-3d exist in mixed oxidation states (Ce^{3+} and Ce^{4+}). It can be observed that the formation of NiO–LS, NiO–SDC, and LS–SDC triple heterostructures results in the peak splitting and initiates the peak shift of Ce^{3+}. Higher content of Ce^{3+} valence state induces faster charge exchange, facilitating ionic conduction.

In addition, O-1s of each component (SnO_2, LS, NiO, SDC, NLS heterostructure, and NLS–SDC 6:4 multi-heterostructure) were also evaluated. The three overlapping peaks of the O-1s spectra at their respective binding energies are shown in Fig. 4(b). Generally, the ionic conductivity of prepared materials, especially electrolytes, strongly depends on the amount of oxygen vacancies formed. It is generally reported that the lattice oxygen (L_O) with a high XPS peak is assigned to the binding energy range of 528–530 eV [44]. Hereby, different oxygen species are indicated as L_O (represented by O_1) at a binding energy of around 528.6 eV, the surface oxide defect peaks (represented by O_2) in the binding energy of 531–539 eV, and the oxygen species adsorbed on oxygen vacancies as well as hydroxyl groups (–OH) (represented by O_3) in the binding energy of 530–532.8 eV. The elevated oxygen vacancy concentration corroborates the enhanced ionic conductivity in NLS–SDC.

Oxygen ion conduction in solid oxide materials typically occurs via a vacancy-mediated mechanism, where oxygen-deficient materials provide diffusion pathways for enhanced ionic transport. The calculated 63% oxygen vacancy content indicates elevated oxygen vacancy concentration, confirming improved ionic conductivity in NLS–SDC 6:4. Furthermore, accumulated chemisorbed oxygen at NLS–SDC interfaces counteracts oxygen vacancy depletion [45]. Synergistic coupling of these dual effects augments ionic conductivity in NLS–SDC composites. Consequently, rapid ion transport within the heterostructures is facilitated by both surface oxygen defects and chemisorbed oxygen formation. The optimal composite ratio of NLS–SDC 6:4 can be evidenced by the O_2 percentage in the NLS–SDC heterostructure materials with other ratios (Figs. S7(c) and S7(d) in the ESM).

To further investigate the oxygen vacancy content in different materials, electron paramagnetic resonance (EPR) spectroscopy was performed, which provides a direct and highly sensitive method for detecting defect structures characterized by unpaired electrons. The EPR signal intensities of the eight materials follow the order: NLS–SDC (6:4 > 5:5 > 7:3) > SDC > NLS > LS > SnO_2 > NiO. The results are in strong agreement with the oxygen vacancy analysis obtained from XPS, thereby providing mutually consistent evidence. A higher oxygen vacancy concentration can lower the adsorption energy of ions at the heterointerface, which in turn reduces the migration energy barrier and facilitates the ion transport. Detailed calculations supporting this interpretation are presented in the following section.

2.5 Computational investigation of heterojunctions

In this study, a series of DFT calculations was performed using an advanced *ab initio* simulation software package. To handle electronic exchange and correlation effects, the Perdew–Burke–Ernzerhof (PBE) exchange-correlation functional based on the generalized gradient approximation (GGA) was chosen. The kinetic energy cutoff was set to 450 eV to ensure the accuracy of energy convergence. All computational models used a $1 \times 2 \times 1$ *k*-point mesh to sample the Brillouin zone to achieve the desired computational precision. At the same time, an appropriate vacuum region (e.g., 15 Å) was introduced in the *Z*-axis direction to reduce interactions between periodic images. The convergence threshold for electronic self-consistent calculations was strictly set to 10^{-5} eV, while the convergence criterion for ionic relaxation was set to 0.02 eV·Å^{-1}.

The band gap values obtained by the hybrid functional calculations are 3.15 eV for NiO, 3.82 eV for LS, 3.60 eV for SnO_2, and 3.13 eV for SDC, which are highly consistent with the experimental results of ultraviolet–visible (UV–Vis) spectroscopy (please refer to the analysis and Figs. S8 and S9 in the ESM for further details).

Optimized structural models of NiO (200)–LS (110), NiO (200)–SDC (110), and NiO (200)–LS (110)–SDC (110) heterojunctions were constructed using a generalized lattice-matching strategy. The corresponding p–n heterojunction models, based on the optimized crystal structures, are depicted in Figs. 5(a), 5(c), and 5(e), respectively.

A BIEF is formed at the heterointerfaces due to the electronic property differences between p-type NiO and n-type LS/SDC, as quantitatively illustrated by the differential charge density analysis. The resulting atomic-scale charge redistribution induces a local electric field (LEF), which can concurrently modulate charge transport and ion conduction, enhance interfacial redox reactivity, and promote proton migration across the interface, thereby enabling synergistic electron and ion transport [30, 46, 47].

Differential charge density maps (Figs. 5(b), 5(d), and 5(f)) reveal significant charge accumulation on the NiO side and depletion on the LS and SDC sides. Bader charge analysis further quantifies the net charge transfer: 0.90|e| from SDC to NiO in NiO–SDC, 3.08|e| from LS to NiO in NiO–LS, and 4.12|e| from LS to NiO in the ternary NiO–LS–SDC system. According to the references [30, 46, 47], the LEF generated by this charge redistribution can effectively reduce the ion migration barrier, and therefore promotes the ion transport along the grain boundaries and via oxygen vacancies.

To gain deeper insights into the interfacial ion migration behavior, this study tried to evaluate the oxygen vacancy formation energy and ionic migration barrier in different heterojunction systems. As shown in Fig. 5(g), the oxygen vacancy formation energies on the NiO side in the NiO–LS and NiO–LS–SDC systems were calculated to be 2.57 and 1.97 eV, respectively, as an example. This indicates that the ternary system facilitates the formation of oxygen vacancies more readily. Bader charge analysis reveals more pronounced charge transfer in the p–n–n heterostructure, suggesting significant electron redistribution at the interface. Such enhanced charge transfer is supposed to be highly related to the reduction of the oxygen vacancy formation energy.

Furthermore, the calculated oxygen ion migration barriers (Figs. 5(h) and 5(i)) for the NiO–SDC and NiO–LS systems are 1.734 and 0.940 eV, respectively, indicating superior ionic migration kinetics in the NiO–LS system. Differential charge density analysis combined with Bader charge calculations shows that the charge redistribution at the NiO–LS interface is significantly greater than that at the NiO–SDC interface, reflecting the possible formation of a stronger BIEF in the former. Along with the higher concentration of oxygen vacancies evidenced by XPS and EPR characterization, and the calculated decreased oxygen vacancy formation energy, these effects together lead to a lower ion migration barrier in the NiO–LS system.

Based on these findings, it can be inferred that in the ternary NiO–LS–SDC heterojunction, the synergistic coupling between n–n and p–n junctions leads to enhanced charge transfer, a stronger BIEF, and a higher concentration of oxygen vacancies. These factors are expected to further optimize the ion migration pathways and achieve an even lower migration barrier.

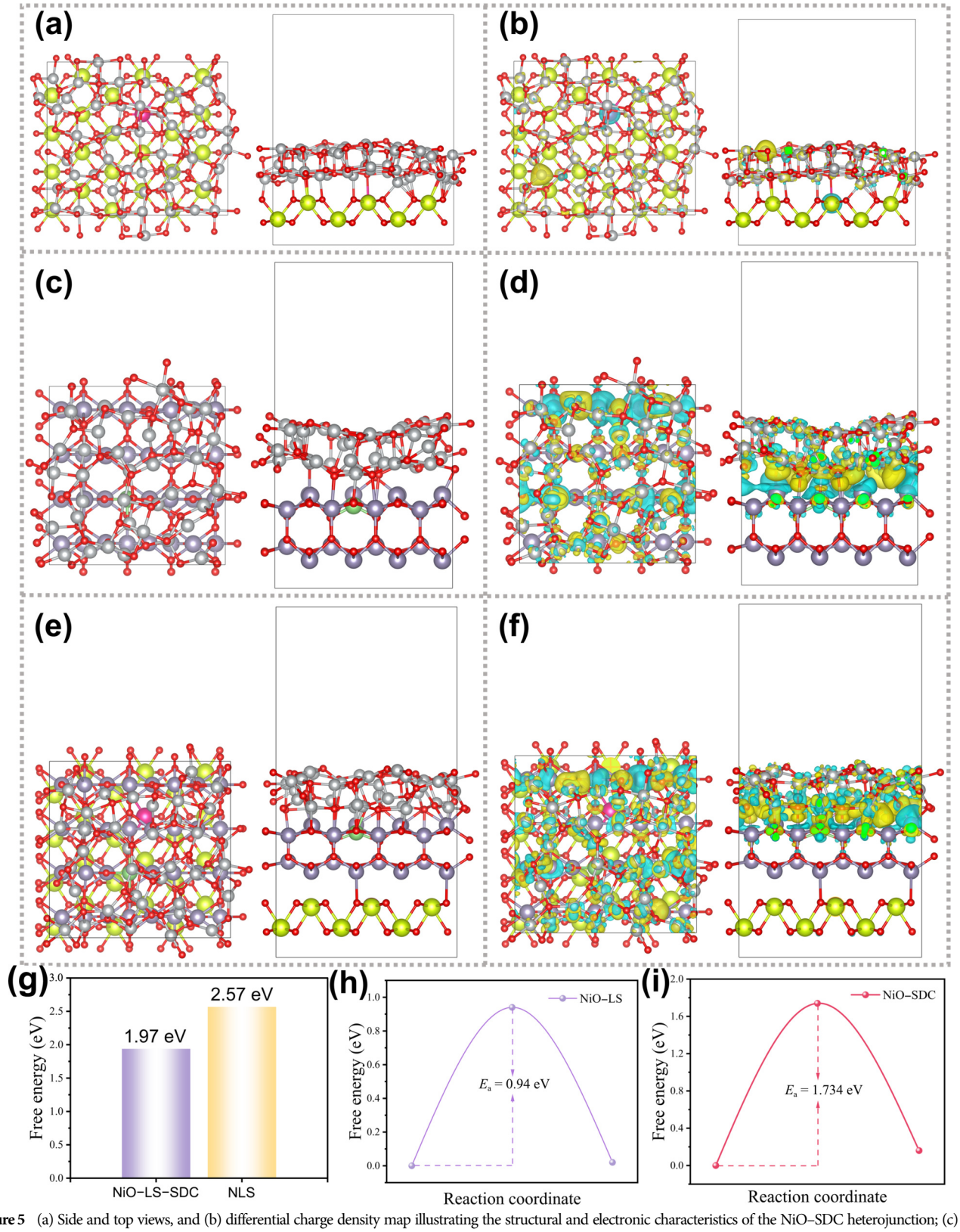

Figure 5 (a) Side and top views, and (b) differential charge density map illustrating the structural and electronic characteristics of the NiO–SDC heterojunction; (c) side and top views, and (d) differential charge density map displaying the features of the NiO–LS heterojunction; (e) side and top views, and (f) differential charge density map presenting the configuration and charge distribution of the NiO–LS–SDC ternary heterojunction. Yellow and cyan regions represent charge accumulation and depletion. Bader charge analysis indicates: In the NiO–SDC heterojunction, the charge transfer amounts are 0.90|e| from NiO to LS and 3.08|e| from NiO to SDC; whereas in the ternary heterojunction, the charge transfer from NiO to LS reaches 4.12|e|. (g) The calculated formation energy of oxygen vacancy in NiO at different heterostructure composites. Oxygen migration energy barriers at the heterointerfaces of (h) NiO–LS and (i) NiO–SDC. Ni, Sn, Li, Sm, Ce, and O elements are represented by yellow, purple, green, gray, red, and blue spheres.

2.6 Energy band structure regulation through heterojunction formation

Focusing on the tunability of the optical–electrical properties of semiconductor materials based on the band alignment strategy via interfacial coupling, this work designs the ternary heterostructure systems (NiO–LS, NiO–SDC, and LS–SDC) to deeply reveal the microscopic mechanism of band engineering. The essence of this work lies in utilizing the interfacial interaction of semiconductor oxide particles with different conductive types to directionally induce the formation of higher level of oxygen vacancy defects in the heterojunction system. An UV–Vis absorption spectroscopy and an ultraviolet photoelectron spectroscopy (UPS) were adopted to evaluate and verify the band regulation mechanism. By accurately determining the band gap and valence band maximum (VBM, V_{BM}) position of each component material (specific values are shown in Figs. 6(a) and 6(c)), it intuitively demonstrates the band alignment characteristics of the heterojunction interface. Specifically, two p–n heterojunctions and one n–n heterojunction were constructed using NiO, SDC, and LS, respectively (Fig. 6(b)). A BIEF is formed through the interface band bending effect.

First, quantitative analysis of optical absorption properties based on the Tauc equation (Eq. (5)) is performed to calculate the band gaps (E_g) of NiO, SnO_2, LS, and SDC from optical absorption spectra [48, 49]

$$\alpha h\nu = \beta_0 (h\nu E_g)^n \tag{5}$$

where α represents the absorption coefficient, $h\nu$ denotes the photon energy, and β_0 is the energy-independent constant. The n value is determined by the semiconductor type (typically, n = 1/2 for direct bandgap, n = 2 for indirect bandgap).

UV–Vis absorption spectroscopy analysis shows that NiO and LS monomers exhibit indirect band gap characteristics of 3.1 and 3.81 eV, respectively, with their absorption edges located at 400 and 320 nm. When the NiO–LS heterojunction is formed, the interface electron coupling effect causes the absorption edge to red-shift to 340 nm, with the corresponding band gap optimized to 3.59 eV (Fig. 6(c)). Similarly, the absorption edge of the NLS–SDC system adjusts from 340 nm (NLS) and 380 nm (SDC) of the monomers to 350 nm, with the band gap value changing to 3.33 eV accordingly (Fig. S10 in the ESM). This band gap narrowing effect originates from the formation of intermediate energy levels induced by interfacial oxygen vacancies, which, as ladder states for electron transitions, significantly reduce the effective band gap width.

The V_{BM} determined by XPS measurements is presented in Fig. S11 in the ESM, as discussed in the corresponding analysis in the ESM. In addition, the maximum value of the valence band was tested by UPS technology, as shown in the following Eq. (6) [50]

$$E_{VB} = 21.2\ \text{eV} - (E_{cutoff} - E_{offset}) \tag{6}$$

The equation includes E_{cutoff} and E_{offset}, which are the higher and lower binding energies from the original data obtained by UPS characterization, as shown in Fig. 5(c) and Fig. S12 in the ESM. The UPS further reveals the evolution of the valence band structure. The V_{BM} of NiO, LS, and SDC are determined to be 7.08, 7.07, and

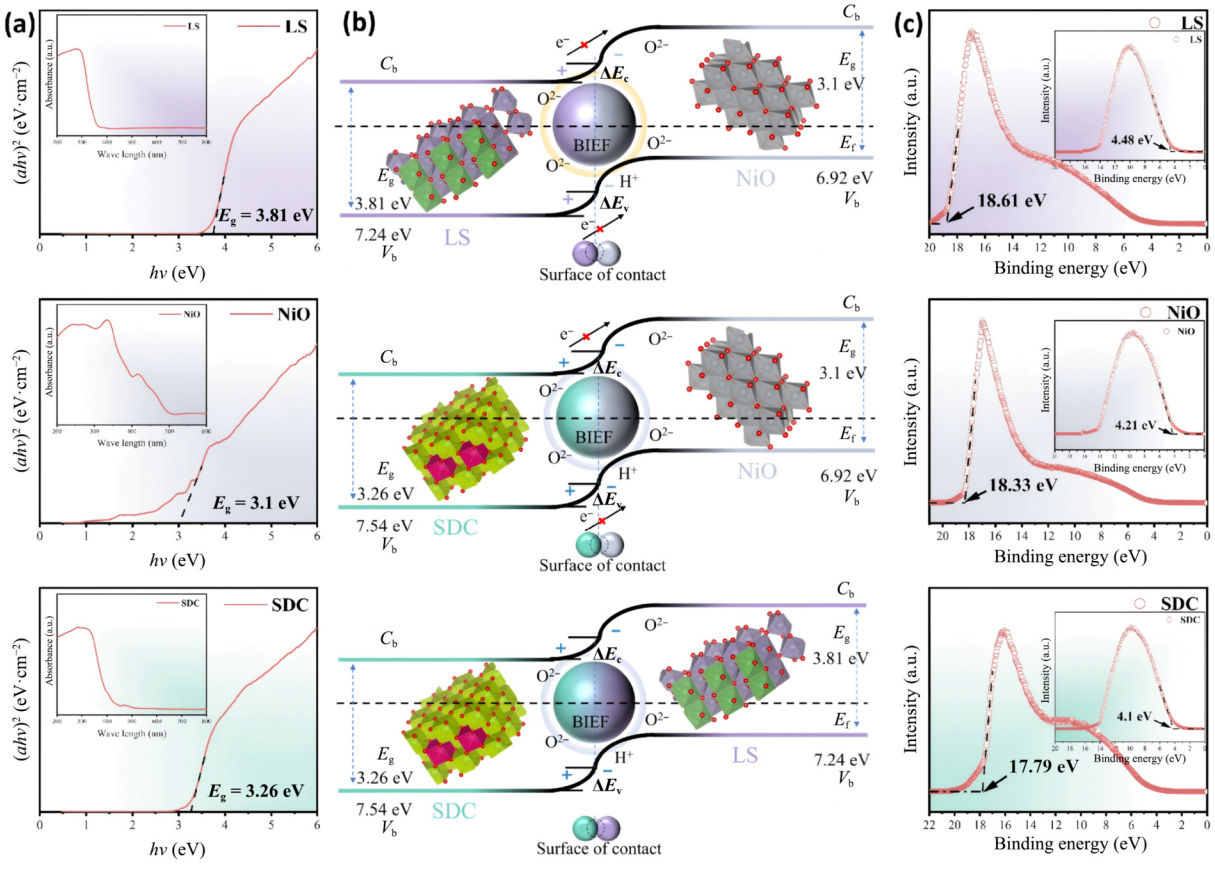

Figure 6 (a) Absorption spectra of NiO, LS, and SDC obtained via ultraviolet–visible spectroscopy and their corresponding bandgap energies. (b) Energy band alignment diagrams of NiO–LS, NiO–SDC, and LS–SDC heterojunctions were constructed based on the bandgap energies and V_{BM} of NiO, LS, and SDC. (c) Valence band positions of NiO, LS, and SDC measured by UPS.

7.40 eV, respectively. Combined with the optical band gap calculation, the conduction band minima (C_{BM}) positions are obtained as 3.92, 3.27, and 4.20 eV. After heterojunction formation, the Fermi level is leveled even at the interface, causing the band bending and forming a space charge region. Its barrier height effectively regulates the charge carrier transport behavior [32].

Upon contact between p-type NiO and n-type LS/SDC, the difference in Fermi levels drives electron diffusion from the n-type to the p-type region, while holes migrate in the opposite direction until thermal equilibrium is attained. This charge redistribution establishes a BIEF directed from the n-type to the p-type side, whose strength seems to be positively correlated with the oxygen vacancy concentration [51, 52]. This field not only promotes the unidirectional migration of ions but also suppresses the electronic conduction pathways, thereby mitigating short-circuit effects. Similarly, when n-type LS and SDC come into contact, electrons spontaneously transfer from the material with the higher Fermi level (LS) to that with the lower Fermi level (SDC), leading to the formation of a space charge region near the interface and generating a strong, unidirectional BIEF that selectively facilitates the ion migration in the materials [53]. Notably, oxygen vacancies, serving as active sites for ionic transport, establish a positive feedback loop between the vacancy concentration gradient and the extent of band bending.

In the p–n–n heterojunction configuration, the introduction of an n–n junction can substantially enhance the functionality of the conventional p–n junction. The structure comprises a p-type semiconductor sequentially integrated with two n-type semiconductors, where the n–n junction is formed between the n-type components adjacent to the p–n interface [54]. From an energy band perspective, the interfacial charge redistribution induced by the n–n junction further tailors the band bending, and thus increases the BIEF gradient at the p–n junction interface. Meanwhile, the BIEF originating from the n–n junction effectively overlaps with that of the p–n junction, yielding a synergistic enhancement that reinforces the overall charge separation efficiency of the heterostructure [55]. In comparison to a single p–n junction electrolyte, this architecture significantly enhances ionic conductivity while suppressing electronic conduction.

The intensified interfacial band bending reduces the energy barrier for vacancy formation, while the accumulation of vacancies further amplifies the LEF [30, 56]. This self-sustaining polarization effect remarkably improves the ionic conductivity of the electrolyte materials for fuel cells, offering a new design paradigm for developing high-performance SOFCs.

3 Conclusions

In summary, this study demonstrates that multi-heterojunction engineering based on simple oxides provides an effective strategy to address the dual challenges of low ionic conductivity and potential electronic leakage in low-temperature SOFC electrolytes. By combining p-type nickel oxide (NiO) with n-type LS and samarium-doped ceria (SDC), the ternary NLS–SDC composite forms two p–n junctions and one n–n interface, which effectively facilitates ion transport while blocking electron conduction. The optimized NLS–SDC 6:4 composite exhibits outstanding performance at 550 °C: a PPD of 916 mW·cm^{-2}, an ionic conductivity of 0.348 S·cm^{-1}, and stable operation for over 280 h at 150 mA·cm^{-2}, significantly surpassing the conventional single-phase or binary systems. Mechanistic insights derived from spectroscopic characterization and DFT calculations reveal that interfacial band alignment and oxygen vacancy enrichment act synergistically to promote the oxygen ion transport through the ternary composite electrolyte. This work thus establishes a conceptually and practically viable pathway toward durable, high-performance electrolytes for sustainable energy conversion.

Electronic Supplementary Material: Supplementary material (the experimental synthesis of NiO, LS, and their composites (NLS and NLS–SDC), the construction of fuel cells with NCAL electrodes, the comprehensive materials characterization (XRD, SEM-EDX, TEM-EDX, XPS, Raman, EIS, and UPS), and the methodology for the DFT + Hubbard correction term (*U*) calculations) is available in the online version of this article at https://doi.org/10.26599/NR.2026.94908331.

Data availability

All data needed to support the conclusions in the paper are presented in the manuscript and the Electronic Supplementary Material. Additional data related to this paper may be requested from the corresponding author upon request.

Acknowledgements

This work is supported by the Guangxi Natural Science Foundation (No. 2025GXNSFAA069080) and the Special Fund for Science and Technology Development of Guangxi (No. AD25069078).

Declaration of competing interest

All the contributing authors report no conflict of interests in this work.

Author contribution statement

T. D. G. was in charge of all experimental work, from material selection and sample preparation to cell assembly, performance measurement, characterization, data analysis, mechanism study, and initial draft writing. Z. W. W. carried out and refined the DFT calculations and contributed to mechanistic interpretation. W. L. L. assisted with the assembly and testing of a subset of cells. J. T. P. and X. M. H. performed portions of the SEM/TEM characterization and data analysis. X. Y. C. conceived the study and supervised the entire project. M. R. C., I. S., and X. T. consulted on the test fixture design. X. J. L. provided guidance on the DFT work and reviewed the manuscript. All authors have reviewed and approved the final manuscript.

Use of AI statement

None.

References

[1] Staffell, I.; Scamman, D.; Abad, A. V.; Balcombe, P.; Dodds, P. E.; Ekins, P.; Shah, N.; Ward, K. R. The role of hydrogen and fuel cells in the global energy system. *Energy Environ. Sci.* **2019**, *12*, 463–491.

[2] Mahato, N.; Banerjee, A.; Gupta, A.; Omar, S.; Balani, K. Progress in material selection for solid oxide fuel cell technology: A review. *Prog. Mater. Sci.* **2015**, *72*, 141–337.

[3] Buonomano, A.; Calise, F.; d'Accadia, M. D.; Palombo, A.; Vicidomini, M. Hybrid solid oxide fuel cells-gas turbine systems for combined heat and power: A review. *Appl. Energy* **2015**, *156*, 32–85.

[4] Nechache, A.; Hody, S. Alternative and innovative solid oxide electrolysis cell materials: A short review. *Renew. Sustain. Energy Rev.* **2021**, *149*, 111322.

[5] Shah, M. A. K. Y.; Lund, P. D.; Zhu, B. Toward next-generation fuel cell materials. *iScience* **2023**, *26*, 106869.

[6] Zhu, B.; Raza, R.; Abbas, G.; Singh, M. An electrolyte-free fuel cell constructed from one homogenous layer with mixed conductivity. *Adv. Funct. Mater.* **2011**, *21*, 2465–2469.

[7] Nie, X. Y.; Chen, Y.; Mushtaq, N.; Rauf, S.; Wang, B. Y.; Dong, W. J.; Wang, X. Y.; Wang, H.; Zhu, B. The sintering temperature effect on electrochemical properties of $Ce_{0.8}Sm_{0.05}Ca_{0.15}O_{2-\delta}$ (SCDC)–$La_{0.6}Sr_{0.4}Co_{0.2}Fe_{0.8}O_{3-\delta}$ (LSCF) heterostructure pellet. *Nanoscale Res. Lett.* **2019**, *14*, 162.

[8] Nie, X. Y.; Zheng, D.; Chen, Y.; Wang, B. Y.; Xia, C.; Dong, W. J.; Wang, X. Y.; Wang, H.; Zhu, B. Processing SCNT ($SrCo_{0.8}Nb_{0.1}Ta_{0.1}O_{3-\delta}$)–SCDC ($Ce_{0.8}Sm_{0.05}Ca_{0.15}O_{2-\delta}$) composite into semiconductor-ionic membrane fuel cell (SIMFC) to operate below 500 °C. *Int. J. Hydrogen Energy* **2019**, *44*, 31372–31385.

[9] Bibi, B.; Nazar, A.; Zhu, B.; Yang, F.; Yousaf, M.; Raza, R.; Shah, M. A. K.; Kim, J. S.; Afzal, M.; Lei, Y. P. et al. Emerging semiconductor ionic materials tailored by mixed ionic–electronic conductors for advanced fuel cells. *Adv. Powder Mater.* **2024**, *3*, 100231.

[10] Shah, M. A. K. Y.; Lu, Y. Z.; Mushtaq, N.; Singh, M.; Rauf, S.; Yousaf, M.; Zhu, B. ZnO/MgZnO heterostructure membrane with type II band alignment for ceramic fuel cells. *Energy Mater.* **2022**, *2*, 200031.

[11] Chen, M. R.; Guo, Y. M.; Xu, J. G.; Wu, J. J.; Tang, X. Intermediate-temperature solid oxide fuel cells based on heterostructure p-type $Sr_2Nb_{1.9}Ti_{0.1}O_{7-\delta}$ microplates and n-type ZnO nanoparticles. *ACS Appl. Nano Mater.* **2024**, *7*, 628–637.

[12] Ru, Y. X.; Chen, Y. J.; Yu, X. Y.; Zhang, Q. Y.; Yin, Y. J.; Tian, G. H. Multipath charge transfer in Cu-BTC@CuS@CeO_2 double p–n heterojunction hollow octahedrons for enhanced photocatalytic amine oxidation. *Chem. Eng. J.* **2023**, *475*, 146158.

[13] Jadhav, A. R.; Bui, V. Q.; Cho, Y.; Liu, Y.; Kumar, A.; Kim, H.; Ajmal, S.; Liu, X. H.; Saqlain, S.; Lee, J. et al. Unveiling a three phase mixed heterojunction via phase-selective anchoring of polymer for efficient photocatalysis. *Adv. Energy Mater.* **2022**, *12*, 2102116.

[14] Mushtaq, N.; Lu, Y. Z.; Xia, C.; Dong, W. J.; Wang, B. Y.; Shah, M. A. K. Y.; Rauf, S.; Akbar, M.; Hu, E. Y.; Raza, R. et al. Promoted electrocatalytic activity and ionic transport simultaneously in dual functional $Ba_{0.5}Sr_{0.5}Fe_{0.8}Sb_{0.2}O_{3-\delta}$–$Sm_{0.2}Ce_{0.8}O_{2-\delta}$ heterostructure. *Appl. Catal. B: Environ.* **2021**, *298*, 120503.

[15] Wang, H. M.; Li, C. H.; Fang, P. F.; Zhang, Z. L.; Zhang, J. Z. Synthesis, properties, and optoelectronic applications of two-dimensional MoS_2 and MoS_2-based heterostructures. *Chem. Soc. Rev.* **2018**, *47*, 6101–6127.

[16] Zhang, K.; Wang, L. Y.; Kim, J. K.; Ma, M.; Veerappan, G.; Lee, C. L.; Kong, K. J.; Lee, H.; Park, J. H. An order/disorder/water junction system for highly efficient co-catalyst-free photocatalytic hydrogen generation. *Energy Environ. Sci.* **2016**, *9*, 499–503.

[17] Xu, Q. L.; Zhang, L. Y.; Cheng, B.; Fan, J. J.; Yu, J. G. S-scheme heterojunction photocatalyst. *Chem* **2020**, *6*, 1543–1559.

[18] Tang, B.; Ji, Q. Q.; Zhang, X. L.; Shi, R. C.; Ma, J.; Zhuang, Z. C.; Sun, M.; Wang, H. J.; Liu, R. Q.; Liu, H. J. et al. Symmetry breaking of FeN_4 moiety via edge defects for acidic oxygen reduction reaction. *Angew. Chem., Int. Ed.* **2025**, *64*, e202424135.

[19] Chen, Y. X.; Meng, Z. H.; Wei, X. L.; Wu, M. J.; Xiong, Y. F.; Tang, H. B.; Wang, R.; Tian, T.; Wang, D. S.; Tang, H. L. Tellurium–nitrogen–carbon support boosting platinum catalysis in high-efficiency proton exchange membrane fuel cells. *Angew. Chem., Int. Ed.* **2025**, *64*, e202512315.

[20] Zhang, M. Y.; Zhu, W.; Liu, Z. Y.; Chen, S. R.; Zhou, D. Y.; Mu, X. Q.; Zhuang, Z. C.; Wang, S. C.; Yang, J. R.; Du. Y. P. et al. Selective sieving effect of multi-atomic bismuth interfaces for efficient formate electrosynthesis and evolution at industrial current density. *Angew. Chem., Int. Ed.* **2025**, *64*, e202510206.

[21] Cao, P. P.; Mu, X. Q.; Chen, F. J.; Wang, S. C.; Liao, Y. R.; Liu, H.; Du, Y. P.; Li, Y. X.; Peng, Y. D.; Gao, M. Z. et al. Breaking symmetry for better catalysis: Insights into single-atom catalyst design. *Chem. Soc. Rev.* **2025**, *54*, 3848–3905.

[22] Mu, X. Q.; Yuan, Y. T.; Yu, M.; Hu, Y. J.; Zeng, W. H.; Peng, W.; Zhang, Y. F.; Liu, X. Y.; Liu, S. L.; Mu, S. C. Robust water/seawater-electrolysis hydrogen production at industrial-scale current densities by modulating built-in-outer electric field of catalytic substance. *Nano Energy* **2024**, *131*, 110216.

[23] Deus, R. C.; Cilense, M.; Foschini, C. R.; Ramirez, M. A.; Longo, E.; Simões, A. Z. Influence of mineralizer agents on the growth of crystalline CeO_2 nanospheres by the microwave-hydrothermal method. *J. Alloys Compd.* **2013**, *550*, 245–251.

[24] Liu, L.; Liu, Y. Y.; Li, L. Y.; Wu, Y.; Singh, M.; Zhu, B. The composite electrolyte with an insulation Sm_2O_3 and semiconductor NiO for advanced fuel cells. *Int. J. Hydrogen Energy* **2018**, *43*, 12739–12747.

[25] Yang, H. M.; Dong, J. G.; Gao, X. N.; Ni, C. M.; Li, Z.; Liu, Y. Y.; Li, J.; He, X. Y.; Tan, W. Y.; Feng, L. G. et al. Modulating built-in electric field via N-doped carbon dots for robust oxygen evolution at large current density. *Small* **2025**, *21*, 2410399.

[26] Zhang, X. F.; Lai, Z. P.; Ye, Y. P.; Su, X. J.; Xie, H. L.; Wu, Y. H.; Li, K. Q.; Wu, W. J. Heterointerface engineering of hollow CoP/CeO_2 p–n heterojunction for efficient electrocatalytic oxygen evolution. *Surf. Interfaces* **2024**, *48*, 104227.

[27] Luo, Y. K.; Zhang, Y. F.; Xu, X. X.; Chen, J. The construction of built-in electric field in p–n heterojunction for optimized interface and improved oxygen evolution reaction activity. *J. Alloys Compd.* **2025**, *1029*, 180795.

[28] Rauf, S.; Hanif, M. B.; Wali, F.; Tayyab, Z.; Zhu, B.; Mushtaq, N.; Yang, T. T.; Khan, K.; Lund, P. D.; Motola, M. et al. Highly active interfacial sites in SFT–SnO_2 heterojunction electrolyte for enhanced fuel cell performance via engineered energy bands: Envisioned theoretically and experimentally. *Energy Environ. Mater.* **2024**, *7*, e12606.

[29] Mushtaq, N.; Lu, Y. Z.; Xia, C.; Dong, W. J.; Wang, B. Y.; Wang, X. Y.; Shah, M. A. K. Y.; Rauf, S.; Nie, J. J.; Hu, E. Y. et al. Design principle and assessing the correlations in Sb-doped $Ba_{0.5}Sr_{0.5}FeO_{3-\delta}$ perovskite oxide for enhanced oxygen reduction catalytic performance. *J. Catal.* **2021**, *395*, 168–177.

[30] Sharif, M. S.; Rauf, S.; Tayyab, Z.; Masood, M. A.; Tian, Y. B.; Shah, M. A. K. Y.; Alodhayb, A. N.; Raza, R.; Zhu, B. High proton conductivity in xCuO/$(1-x)$$CeO_2$ electrolytes induced by CuO self-nucleation and electron–ion coupling. *Adv. Sci.* **2025**, *12*, 2417421.

[31] Xia, C.; Mi, Y. Q.; Wang, B. Y.; Lin, B.; Chen, G.; Zhu, B. Shaping triple-conducting semiconductor $BaCo_{0.4}Fe_{0.4}Zr_{0.1}Y_{0.1}O_{3-\delta}$ into an electrolyte for low-temperature solid oxide fuel cells. *Nat. Commun.* **2019**, *10*, 1707.

[32] Lee, S.; Zhang, W. R.; Khatkhatay, F.; Wang, H. Y.; Jia, Q. X.; Macmanus-Driscoll, J. L. Ionic conductivity increased by two orders of magnitude in micrometer-thick vertical yttria-stabilized ZrO_2 nanocomposite films. *Nano Lett.* **2015**, *15*, 7362–7369.

[33] Shah, M. A. K. Y.; Mushtaq, N.; Rauf, S.; Xia, C.; Zhu, B. The semiconductor $SrFe_{0.2}Ti_{0.8}O_{3-\delta}$–ZnO heterostructure electrolyte fuel cells. *Int. J. Hydrogen Energy* **2019**, *44*, 30319–30327.

[34] Zhu, B.; Fan, L. D.; Mushtaq, N.; Raza, R.; Sajid, M.; Wu, Y.; Lin, W. F.; Kim, J. S.; Lund, P. D.; Yun, S. N. Correction to: Semiconductor electrochemistry for clean energy conversion and storage. *Electrochem. Energy Rev.* **2023**, *6*, 25.

[35] Asghar, M. I.; Jouttijärvi, S.; Jokiranta, R.; Valtavirta, A. M.; Lund, P.

D. Wide bandgap oxides for low-temperature single-layered nanocomposite fuel cell. *Nano Energy* **2018**, *53*, 391–397.

[36] Rauf, S.; Hanif, M. B.; Tayyab, Z.; Veis, M.; Shah, M. A. K. Y.; Mushtaq, N.; Medvedev, D.; Tian, Y. B.; Xia, C.; Motola, M. et al. Alternative strategy for development of dielectric calcium copper titanate-based electrolytes for low-temperature solid oxide fuel cells. *Nano-Micro Lett.* **2025**, *17*, 23.

[37] Su, Q.; Yoon, D.; Chen, A. P.; Khatkhatay, F.; Manthiram, A.; Wang, H. Y. Vertically aligned nanocomposite electrolytes with superior out-of-plane ionic conductivity for solid oxide fuel cells. *J. Power Sources* **2013**, *242*, 455–463.

[38] Yeetsorn, R.; Petrone, R.; Hissel, D.; Harel, F.; Bervas, E.; Gao, F.; Prea, M. C. Influence of cycle repetition on stack voltage degradation during fuel cell stress tests. *Fuel Cells* **2022**, *22*, 85–101.

[39] Rauf, S.; Shah, M. A. K. Y.; Zhu, B.; Tayyab, Z.; Ali, N.; Attique, S.; Xia, C.; Khatoon, R.; Yang, C. P. Asghar, M. I. et al. Electrochemical properties of a dual-ion semiconductor-ionic $Co_{0.2}Zn_{0.8}O$–$Sm_{0.20}Ce_{0.80}O_{2-\delta}$ composite for a high-performance low-temperature solid oxide fuel cell. *ACS Appl. Energy Mater.* **2021**, *4*, 194–207.

[40] Zhang, Y. F.; Liu, J. J.; Singh, M.; Hu, E. Y.; Jiang, Z.; Raza, R.; Wang, F. Z.; Wang, J.; Yang, F.; Zhu, B. Superionic conductivity in ceria-based heterostructure composites for low-temperature solid oxide fuel cells. *Nano-Micro Lett.* **2020**, *12*, 178.

[41] Barr, T. L. *Modern ESCA: The Principles and Practice of X-Ray Photoelectron Spectroscopy*; CRC Press: Boca Raton, **1994**.

[42] Li, Z. J.; Ma, Q.; Li, Z. Z.; Zhang, D.; Sun, Q. J.; Wang, Q. J.; Sun, H. L.; Wang, B. Exploring the role of solvents in structural regulation during ultrasonic synthesis of Co/Ni-layered double hydroxide for oxygen evolution reaction. *Mater. Rep.: Energy* **2024**, *4*, 100296.

[43] Zhao, X. Y.; Ren, Y. C.; Jiang, R. L.; Liu, J. X.; Zhang, J.; Liu, W.; Wang, Z. P. Performance and mechanism of cerium–praseodymium–manganese ($CePrMnO_x$) solid solution in catalytic soot combustion. *China Powder Sci. Technol.* **2025**, *31*, 174–186.

[44] Gao, T. F.; Kumar, A.; Shang, Z. C.; Duan, X. X.; Wang, H. C.; Wang, S. Y.; Ji, S. F.; Yan, D. P.; Luo, L.; Liu, W. et al. Promoting electrochemical conversion of CO_2 to formate with rich oxygen vacancies in nanoporous tin oxides. *Chin. Chem. Lett.* **2019**, *30*, 2274–2278.

[45] Ganesh, K. S.; Wang, B. Y.; Kim, J. S.; Zhu, B. Ionic conducting properties and fuel cell performance developed by band structures. *J. Phys. Chem. C* **2019**, *123*, 8569–8577.

[46] Zhang, Y. X.; Chen, Y.; Lin, Y.; Yan, M. F.; Harris, W. M.; Chiu, W. K. S.; Ni, M.; Chen, F. L. Electrochemical fields within 3D reconstructed microstructures of mixed ionic and electronic conducting devices. *J. Power Sources* **2016**, *331*, 167–179.

[47] Li, W. Y.; Guan, B.; Yang, T.; Zhang, N.; Zhang, X. X.; Liu, X. B. On the bulk transport process and its impact on the electrode behavior of mixed conducting electrodes for SOFCs. *Phys. Chem. Chem. Phys.* **2017**, *19*, 23218–23228.

[48] Cordell, J. J.; Pan, J.; Tamboli, A. C.; Tucker, G. J.; Lany, S. Bandgap analysis and carrier localization in cation-disordered $ZnGeN_2$. *APL Mater.* **2022**, *10*, 011112.

[49] Samreen, A.; Ali, M. S.; Huzaifa, M.; Ali, N.; Hassan, B.; Ullah, F.; Ali, S.; Arifin, N. A. Advancements in perovskite-based cathode materials for solid oxide fuel cells: A comprehensive review. *Chem. Rec.* **2024**, *24*, e202300247.

[50] Zhang, Y B.; Zhu, D. C.; Jia, X.; Liu, J. M.; Li, X. F.; Ouyang, Y. Z.; Li, Z.; Gao, X. W.; Zhu, C. J. Novel n–i CeO_2/a-Al_2O_3 heterostructure electrolyte derived from the insulator a-Al_2O_3 for fuel cells. *ACS Appl. Mater. Interfaces* **2023**, *15*, 2419–2428.

[51] Zhao, D.; Yan, R.; Mushtaq, N.; Wu, J. E.; Shah, M. A. K. Y.; Li, H. H.; Lu, Y. Z.; Wang, P. Developing the fast ionic transport in the semiconductor ionic heterostructure composed of $La_{0.8}Sr_{0.2}Co_{0.8}Fe_{0.2}$–$Gd_{0.1}Ce_{0.9}O_2$ for the electrolyte application in ceramic fuel cells. *Crystals* **2023**, *13*, 697.

[52] Ma, W. Q.; Jian, T. Z.; Ma, J. P.; Li, X. H.; Gao, H. Y.; Liu, H. Research progress on transition metals and their alloy catalysts for Li–CO_2 batteries. *China Powder Sci. Technol.* **2024**, *30*, 1–14.

[53] Yue, F.; Fan, Z. Y.; Li, C.; Meng, Y.; Zhang, S.; Shi, M. K.; Wang, M. H.; Berrettoni, M.; Li, J.; Zhang, H. Z. Electro-assisted photocatalytic reduction of CO_2 in ambient air using Ag/TNTAs at the gas–solid interface. *Mater. Rep.: Energy* **2024**, *4*, 100269.

[54] Hu, H. X.; Liang, H. Y.; Liu, X. Y.; Jiang, H. H.; Yi, M. Y.; Wu, Y. Z.; Hao, X. P.; Chang, B.; Zhou, W. J. Optimization of single crystal surface and interface structures for electrocatalysis. *Mater. Rep.: Energy* **2025**, *5*, 100358.

[55] Zhang, H. B.; Wang, C. J. Photothermal synergistic catalysis and associated kinetics. *China Powder Sci. Technol.* **2025**, *31*, 11–21.

[56] Wei, T. C.; Zhou, J.; An, X. Q. Recent advances in single-atom catalysts (SACs) for photocatalytic applications. *Mater. Rep.: Energy* **2024**, *4*, 100285.